HYDROGELS

N-type semiconducting hydrogel

Peiyun Li[1]†, Wenxi Sun[1]†, Jiulong Li[1], Ju-Peng Chen[1], Xinyue Wang[2], Zi Mei[3], Guanyu Jin[1], Yuqiu Lei[4], Ruiyun Xin[5], Mo Yang[2], Jingcao Xu[1], Xiran Pan[1], Cheng Song[4], Xin-Yu Deng[1], Xun Lei[1], Kai Liu[1], Xiu Wang[1], Yuting Zheng[4], Jia Zhu[5], Shixian Lv[1], Zhi Zhang[1], Xiaochuan Dai[2], Ting Lei[1]*

Hydrogels are an attractive category of biointerfacing materials with adjustable mechanical properties, diverse biochemical functions, and good ionic conductivity. Despite these advantages, their application in electronics has been restricted because of their lack of semiconducting properties, and they have traditionally only served as insulators or conductors. We developed single- and multiple-network hydrogels based on a water-soluble n-type semiconducting polymer, endowing conventional hydrogels with semiconducting capabilities. These hydrogels show good electron mobilities and high on/off ratios, enabling the fabrication of complementary logic circuits and signal amplifiers with low power consumption and high gains. We demonstrate that hydrogel electronics with good bioadhesive and biocompatible interface can sense and amplify electrophysiological signals with enhanced signal-to-noise ratios.

Hydrogels, composed of three-dimensionally cross-linked hydrophilic polymer networks, are capable of retaining large amounts of water (*1*). Within contrast to rigid inorganic materials and dry polymers, the mechanical properties of hydrogels can be widely adjusted to match various biological tissues, such as cartilage, skin, muscle, and brain (*2*, *3*). The structures of hydrogels are also diverse and easy to modify, showing excellent versatility in biofunctional engineering (*4*). By modifying different functional groups, hydrogels can exhibit stimulus responsiveness (*5*) and attractive interfacial properties (*1*, *6*). This has led to their use in sensors (*7*), actuators (*8*), coatings (*9*), acoustic detectors (*10*), optics (*11*), and electronics (*12*, *13*).

Traditional hydrogels are ionic conductive but lack electronic conductivity (*14*). Their three-dimensional hydrophilic networks make them good ion conductors and satisfactory biocompatible materials. Therefore, hydrogels can effectively reduce the interfacial impedance between traditional metal electrodes and the biological tissue, which is convenient for the collection of biosignals (*15*). However, the low conductance and mobility of ions limit the signal amplitude, response speed, and cutoff frequency of electronics that are based on hydrogels (*16*). To enhance the electronic conductivity of hydrogels, micro- and nanocomposites such as carbon (*17*, *18*) and metal materials (*19*, *20*) have been added to the hydrogel matrix. Conducting polymers offer substantial advantages in terms of mechanical flexibility and biocompatibility (*21*). Therefore, conducting polymers, such as poly(3,4-ethylenedioxythiophene) polystyrene sulfonate (PEDOT:PSS) (*22*–*24*), have been blended with nonconducting hydrogels to create interpenetrating networks. This provides good electronic conductivity to the hydrogel systems, enabling multifunctional electronic devices (*25*).

Semiconductors play crucial roles in electronics, serving as fundamental elements for switching, amplifying, rectifying, and logic operations (*26*, *27*). Hayward *et al.* demonstrated the basic functions of diodes and transistors using ionic heterojunctions, which presented an opportunity for constructing logic circuits by using hydrogels (*28*, *29*). However, the device performance and applications are limited by the low mobility of ions and incompatibility with electronic circuits.

Design and preparation of single-network semiconducting hydrogel

We envisioned that if semiconducting hydrogels could be developed, they could be used to build up circuits similar to conventional semiconductors while maintaining a good interface with tissue (Fig. 1A). Hydrogels are typically formed by cross-linked water-soluble polymers. However, most semiconducting polymers are water insoluble. Although the hydrophilicity of conjugated polymers can be improved by introducing ionic or ethylene glycol chains, they still need to be dissolved in alcohol or chlorinated solvents. The incorporation of cations into the conjugated polymer skeleton can improve water solubility. We designed an n-type water-soluble semiconducting polymer, P(PyV), that possesses a cationic backbone with chloride counterions and does not have any side chains (Fig. 1B and supplementary materials) (*30*). We believe that a side chain–free polymer design could enable high electronic performance (*31*, *32*), and the ionic backbone provides the potential for electrostatic cross-linking. Using density functional theory (DFT) calculations, we found that the binding energy between benzenesulfonate ion and polymer backbone is greater than that of the chloride ion, making the exchange process thermodynamically favorable (fig. S3). We chose disodium 1,3-benzenedisulfonate (DBS) as the cross-linker because it is a dianion, and its small size minimizes effects on electronic properties. When P(PyV) and DBS are mixed, they can form a bulk hydrophilic network that is insoluble in water (Fig. 1, C and F), suggesting that P(PyV) was electrostatically cross-linked to form hydrogel by the dianions.

The cross-linking method facilitates the preparation of hydrogel films. By spin-coating a P(PyV) solution onto a substrate and subsequently immersing in a dimethyl sulfoxide (DMSO) solution of DBS, which is an orthogonal solvent for P(PyV), a P(PyV) hydrogel [P(PyV)-H] thin film can be produced (fig. S4). X-ray photon-electron spectroscopy (XPS) results revealed the disappearance of the chlorine signal and the emergence of the sulfur signal, indicating a complete exchange of the anions (Fig. 1D and fig. S10). The stability of the cross-linked P(PyV)-H was confirmed through ultraviolet–visible–near infrared (UV-vis-NIR) spectra, demonstrating that the hydrogel remains stable even after prolonged soaking in water (Fig. 1E and fig. S5). We examined the morphology of P(PyV)-H using atomic force microscopy (AFM), and the images indicated that the cross-linking process did not visibly affect the film's morphology (fig. S6). Grazing incidence wide-angle x-ray scattering (GIWAXS) showed that the lamellar and π-π stacking distances ($d_{lamellar}$ and $d_{\pi\text{-}\pi}$, respectively) of the hydrogel are slightly enlarged compared with those of the pristine film (table S2 and fig. S7). We freeze-dried the bulk hydrogel to investigate its morphology. Scanning electron microscope (SEM) images showed that the P(PyV)-H has a porous structure, contrasting with the pristine P(PyV) film and other conjugated polymers (Fig. 1F and figs. S8 and S9). These findings confirm that the P(PyV)-H forms a stable three-dimensional porous network structure, similar to traditional hydrogel, which could facilitate water storage and efficient ion and molecules transport.

A patterned P(PyV)-H can be obtained by spray-coating the cross-linker solution onto the film through a shadow mask, followed by rinsing with water to wash away the portion not cross-linked (fig. S4). The resolution of this spray-coating patterning method is about 200 μm (fig. S11), and this patternable capability can simplify the fabrication process of large-size hydrogel-based devices (Fig. 1G).

Semiconducting properties of the P(PyV)-H

Spectroelectrochemistry was performed to investigate the electrochemical characteristics of the hydrogel (fig. S12A). During electrochemical

[1]Key Laboratory of Polymer Chemistry and Physics of Ministry of Education, School of Materials Science and Engineering, Peking University, Beijing 100871, China. [2]Department of Biomedical Engineering, School of Medicine, Tsinghua University, Beijing 100084, China. [3]School and Hospital of Stomatology, Peking University, Beijing 100871, China. [4]College of Engineering, Peking University, Beijing 100871, China. [5]Laboratory of Theoretical and Computational Nanoscience, CAS Center for Excellence in Nanoscience, National Center for Nanoscience and Technology, Chinese Academy of Sciences, Beijing 100190, China.
*Corresponding author. Email: tinglei@pku.edu.cn
†These authors contributed equally to this work.

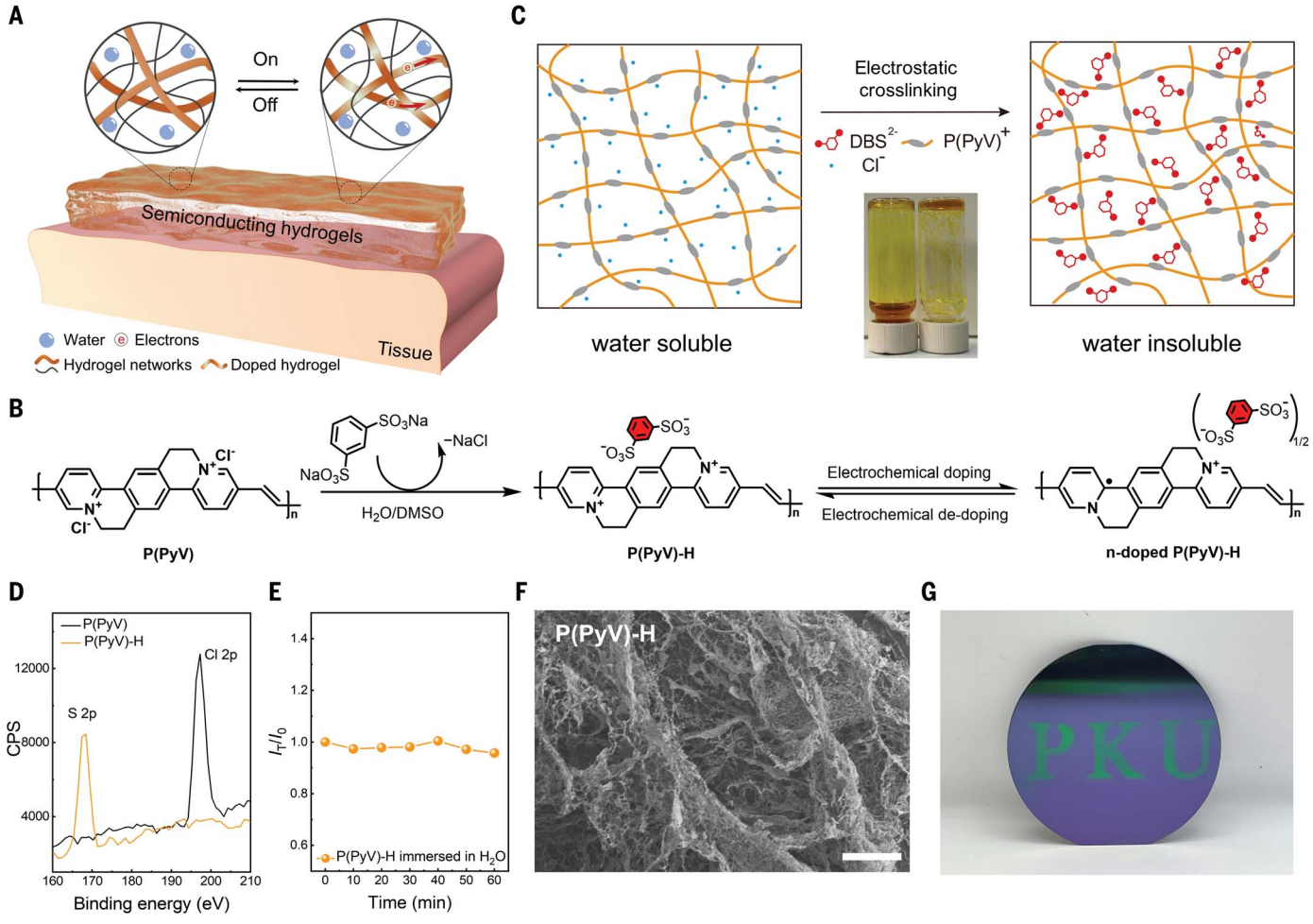

Fig. 1. Single-network semiconducting hydrogel based on P(PyV). (**A**) Conceptual diagram of the working mechanism of semiconducting hydrogel. (**B**) Chemical structure of P(PyV), the dianion exchange reaction, and the electrochemical doping-dedoping processes. (**C**) Schematic illustration of the film microstructure of the pristine and the cross-linked hydrogel. (Inset) Photograph of P(PyV) solution and the bulk P(PyV)-H in bottles. (**D**) Sulfur (2p) and chlorine (2p) XPS spectra of the pristine P(PyV) and the ion-exchanged P(PyV)-H. CPS, counts per second. (**E**) Stability study of the P(PyV)-H immersed in water. I_T, intensity of the maximum absorption peak; I_0, original intensity of the maximum absorption peak. The I_T shows no obvious change in 1 hour, indicating that the cross-linked film is insoluble and stable in water. (**F**) SEM images of freeze-dried P(PyV)-H. Scale bar, 20 μm. (**G**) Photograph of the patterned P(PyV)-H with logo "PKU" on a 2-inch silicon wafer.

reduction, some of the anions leave the P(PyV)-H, leading to an n-doped hydrogel with decreased absorption bands of the pristine polymer (400 to 500 nm) and increased polaron absorption bands (500 to 800 nm) (*33*). The formation of the polaron bands was supported by our chemical doping experiments and DFT calculations (fig. S13). To evaluate the semiconducting properties of P(PyV)-H, we used organic electrochemical transistors (OECTs) (Fig. 2). OECTs can operate in aqueous solution with low operating voltages (usually <1 V) (*34*). The benchmark value μC^*, where μ is the electron mobility and C^* is the volumetric capacitance, of the hydrogel-based OECTs first slightly increased and then decreased as the cross-linking time increased (fig. S12B) (*35*). Therefore, we chose 5 min to be the cross-linking time for further device fabrication and characterization. The P(PyV)-H shows n-type OECT performance, with μC^* values of up to 120 F cm^{-1} V^{-1} s^{-1} (112 ± 6 F cm^{-1} V^{-1} s^{-1}), on/off ratios >10^7, and response times (τ_{on}/τ_{off}) of 1.58/0.18 ms (Fig. 2, B to D). The μC^* values are among the highest in reported n-type semiconducting polymers (fig. S14) (*36*). We measured C^* by use of the electrochemical impedance spectrum (EIS) (fig. S15). The maximal C^* was extracted to be 485 ± 56.3 F cm^{-3}. Such high capacitance value suggests that P(PyV)-H has excellent ion storage and transport capabilities. On the basis of the μC^* and C^* values, μ was calculated to be 0.25 (0.23 ± 0.01) cm^2 V^{-1} s^{-1}, which is comparable with the state-of-the-art n-type OECT materials. The proposed electrochemical doping-dedoping mechanism of P(PyV)-H is illustrated in fig. S18. The hydrogel structure is stable because only 1/3 of the DBS^{2-} was replaced by Cl^- during the electrochemical operation (figs. S16 and S17). After electrochemical doping, the charge carrier density of P(PyV)-H reaches 1.75 × 10^{21} cm^{-3}, which is equivalent to two charges every three repeating units. DFT calculations showed that electrons are delocalized along the polymer backbone (fig. S19). Besides, we calculated the band structures of polymer under pristine and reduced states (fig. S20). Pristine P(PyV) shows a small electron effective mass (m_e^* = 0.157 m_e), suggesting a good theoretical electron mobility along the polymer chain (*37*). In the reduced state, the Fermi level shifted up and surpassed the conduction band minimum (CBM), indicating an electron transport (fig. S21) (*38*).

To evaluate the integration capability of P(PyV)-H, we fabricated complementary inverters and logic circuits (Fig. 2A). Because of the lack of enhancement-mode p-type semiconducting hydrogels, we used for this study a p-type OECT material, P(lgDPP-MeOT2) (*39*).

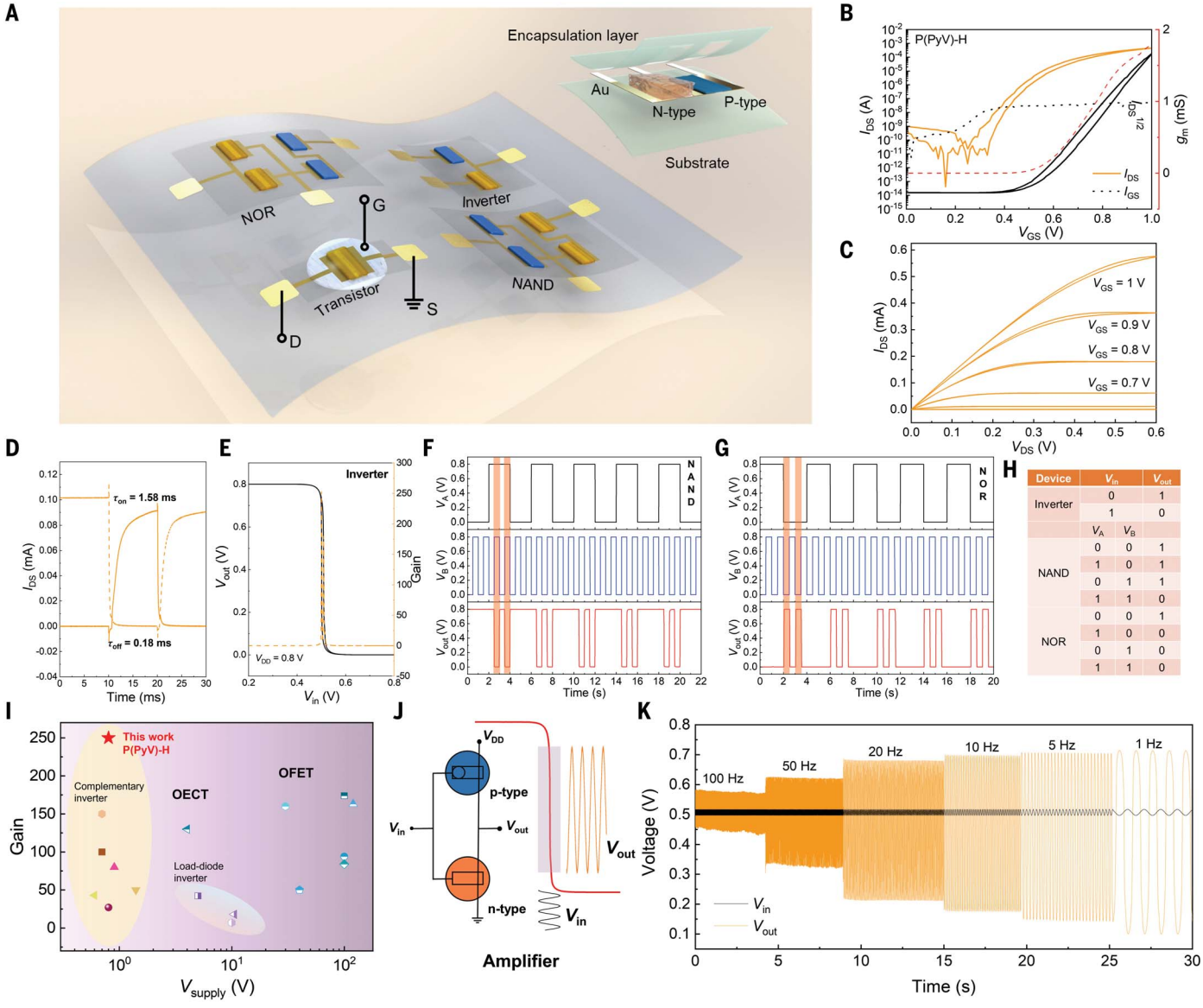

Fig. 2. Semiconducting properties of P(PyV)-H. (**A**) Schematic of the semiconducting hydrogel devices, including a transistor, inverter, NAND, and NOR. "G," "D," and "S" are the gate, drain, and source electrodes, respectively. p-type semiconductors are in blue, and n-type semiconducting hydrogels are in orange. (**B**) Transfer and (**C**) output characteristics of the P(PyV)-H. (**D**) Transient on/off curves with gate-to-source voltage (V_{GS}) of 0 to 1 V. Device configuration is W/L = 100/10 μm and drain-to-source voltage (V_{DS}) = 0.6 V. I_{DS}, drain-to-source current. (**E**) Voltage transfer characteristics and gain of the complementary inverter based on p-type polymer P(lgDPP-MeOT2) and P(PyV)-H. Device configuration is W/L = 100/10 μm. (**F** and **G**) Corresponding voltage input and output characteristics of NAND and NOR. (**H**) The truth table of an inverter, NAND, and NOR gate. (**I**) Comparison of the gain and voltage supply of different types of inverters (*41*–*44*). (**J**) Signal amplification principle of the OECT inverter-based amplifier. (**K**) Dynamic response of small sinusoidal signals with different frequencies of the inverter. The amplitude of the V_{in} is 10 mV.

When the supply voltage (drain voltage; V_{DD}) of the complementary inverter was set to 0.8 V and the input voltage (V_{in}) was swept from 0 to 0.8 V, a high gain value ($\partial V_{out}/\partial V_{in}$) of 250 was obtained (Fig. 2E and fig. S22, A and B), exceeding reported values for both OECTs and organic field-effect transistors (OFETs) (*40*, *41*). The inverter is power-efficient and exhibits a power consumption of <1 μW (fig. S22C). By introducing a two-stage inverter, the gain can be further improved to 385, and power consumption remains at about 1 μW (fig. S22, D and E). NAND and NOR circuits with four transistors were built and showed correct logic functions, demonstrating the potential of using semiconducting hydrogel for constructing integrated circuits (Fig. 2, F to H). Compared with OFET- and other OECT-based inverters, our hydrogel-based complementary inverters show both low operating voltage and high gains (Fig. 2I and table S3) (*41*–*44*). The amplitude of biological electrical signals is typically very small, necessitating the use of sophisticated acquisition and amplification circuits for detection, which presents challenges for wearable monitoring of these signals. Using complementary inverters, we can construct efficient signal amplifiers for low-amplitude biosignals (Fig. 2J). For our hydrogel amplifier, the signal amplification function can be realized from 1 to 100 Hz (Fig. 2K). When a 1-mV sinusoidal signal is input, the magnification could reach 79 at 1 Hz (fig. S22F).

Preparation and properties of multiple-network semiconducting hydrogels

P(PyV)-H can also be blended with other well-developed hydrogels, forming multiple-network hydrogels (MNHs) with enhanced mechanical

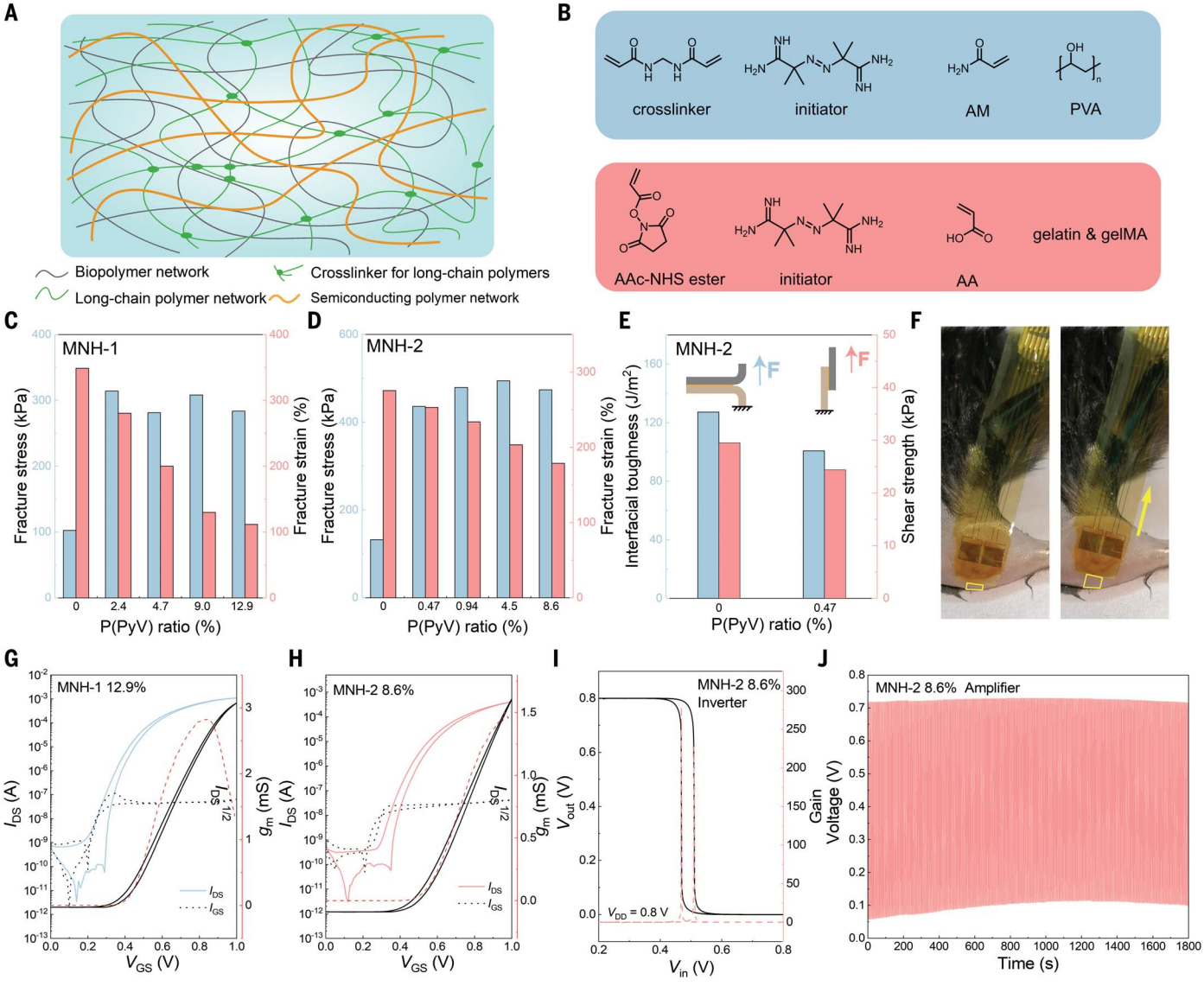

Fig. 3. Preparation and properties of multiple network hydrogels. (**A**) Schematic illustration of the microstructures of the multiple network hydrogels. (**B**) Chemical structures of the components used for constructing multiple network hydrogels: MNH-1 and MNH-2. (**C** and **D**) Comparison of the fracture stress and strain with different P(PyV) ratios in MNH-1 and MNH-2. (Inset) Schematic illustration of the measurement setup. (**E**) Comparison of the interfacial toughness and shear strength after adding P(PyV) in MNH-2. (Inset) Schematic illustration of the measurement setup. The brown bar indicates the pig skin, the gray bar indicates substrate, and the orange bar indicates MNH-2. (**F**) Photographs of OECT devices based on MNH-2 attached to skin tissue. The device fully attached to the skin before and during multiple tensile stress. (**G**) Transfer characteristics of MNH-1 [12.9 wt % P(PyV) polymer]. (**H**) Transfer characteristics of MNH-2 [8.6 wt % P(PyV) polymer]. (**I**) Voltage transfer characteristics and gain of the complementary inverter based on P(IgDPP-MeOT2) and MNH-2 8.6%. Device configuration is W/L = 100/10 μm. (**J**) Dynamic response stability of the amplifier based on MNH-2. The amplitude of the small sinusoidal signals is 10 mV, and the frequency is 1 Hz.

and good bioadhesive properties (Fig. 3, A and B). Two MNH systems are demonstrated. Each system contains three polymer networks: a long-chain polymer network [polyacrylamide (PAM) or polyacrylic acid (PAA)], a biopolymer network [polyvinyl alcohol (PVA) or gelatin], and a semiconducting polymer network [P(PyV)]. Both MNHs were synthesized by means of thermal polymerization and crosslinking in aqueous solutions. MNH-1 incorporates PAM and PVA, exhibiting high tensile strength and hygroscopicity, whereas MNH-2 incorporates PAA, gelatin, gelatin methacrylate (gelMA), and acrylic acid N-hydroxysuccinimide ester (AAc-NHS ester), exhibiting high stretchability and good biointerface adhesion (fig. S24) (*45*). The water content of the MNHs is 60 to 70%, which is greater than that of pure P(PyV)-H (~40%) (fig. S25). The tensile tests showed that the MNHs could exhibit high stretchability, with fracture strains >100%. The fracture stress was acutely increased after adding a small amount of P(PyV) because P(PyV) is stiffer than conventional hydrogels. With further increase in P(PyV), the fracture stress is basically unchanged, but the fracture strain gradually decreases (Fig. 3, C and D, and fig. S24). Previous studies reported that hydrogels containing PAA, gelatin, gelMA, and AAc-NHS exhibited excellent bioadhesive properties (*45*). MHN-2 demonstrated good interfacial toughness (~100 J m^{-2}) and shear strength (25 kPa) on pig skin (Fig. 3E). The presence of multiple-polymer networks and components did not notably affect the semiconducting properties of P(PyV) polymer network. Both MNH-1 and

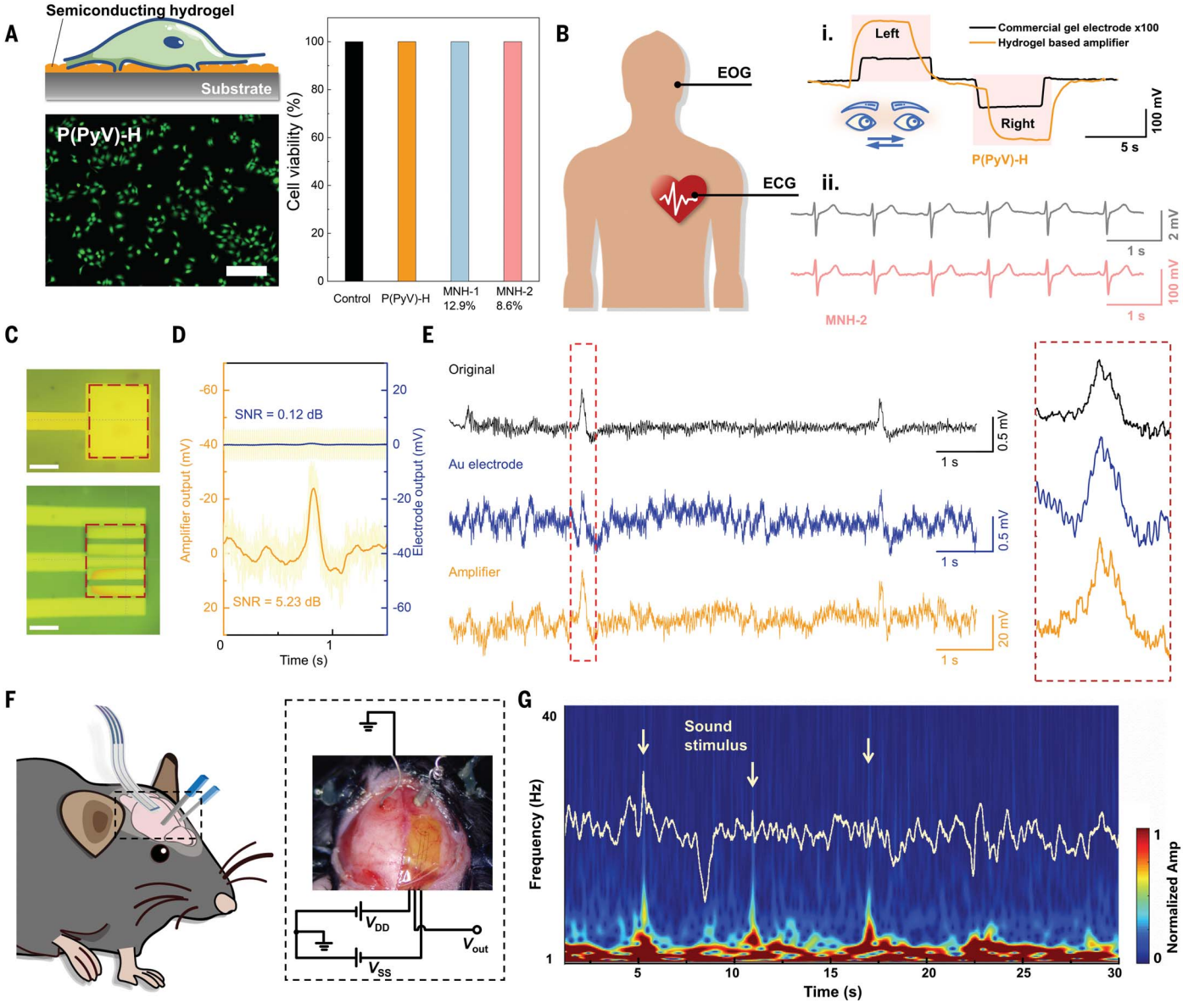

Fig. 4. Applications of the semiconducting hydrogel amplifiers. (**A**) Live/dead staining and cell viability of HaCaTs. Scale bar, 100 μm. (**B**) EOG and ECG signals acquired by hydrogel amplifiers. (i) The associated EOG signals obtained by the amplifier based on P(PyV)-H compared with commercial gel electrode during left-right eye movement. (ii) The precordial leads V2 ECG signals obtained with the amplifier based on MNH-2 compared with commercial gel electrode. The output curve was rectified according to fig. S33. (**C**) Photograph of the Au electrode and amplifier channels with the same effective area. Scale bars, 50 μm. (**D**) Simulated EEG signals and average waveforms measured with Au electrodes and amplifiers on an agar brain model. The SNR of the amplifier signal is much higher than that of the Au electrode. (**E**) Simulated EEG signals measured with gold electrodes and amplifiers compared with the pristine signal. The signals were digitally filtered by using a 50-Hz notch filter. (**F**) Photograph of in vivo ECoG recording and schematic of electrical wiring. (**G**) The time domain ECoG signals obtained by the P(PyV)-H–based flexible amplifier and its time-frequency analysis diagram. Arrows indicate the timing of sound stimuli during ECoG recording.

MNH-2 with various ratios can exhibit good semiconducting characteristics comparable with that of pure P(PyV)-H (Fig. 3, G and H, and fig. S26, A to C). MNH-1 (12.9 wt %) displayed a μC^* value of 13.5 F cm^{-1} V^{-1} s^{-1} (equivalent to 105 F cm^{-1} V^{-1} s^{-1} after conversion by mass ratio), and MNH-2 (8.6 wt %) displayed a μC^* value of 9.72 F cm^{-1} V^{-1} s^{-1} (equivalent to 113 F cm^{-1} V^{-1} s^{-1} after conversion). These results indicate that the semiconducting hydrogel has the potential to form composite materials with other hydrogels without substantial loss in electrical properties. Because of the thicker film, the OECT response time of MNHs is longer than that of P(PyV)-H. The cut-off frequency was about 100 Hz for the MNH-based OECTs (fig. S26, D to F).

The device based on MNH-2 showed much improved bioadhesion when attaching to various mouse tissues such as brain and skin tissues (Fig. 3F and fig. S29). These results suggest that our semiconducting hydrogels could integrate more attractive features of conventional hydrogels while maintaining outstanding electronic performance. The performance of the MNH-2 device remained essentially unchanged after ultrasonic treatment for 1 hour in sodium chloride solution, whereas the device performances of PEDOT:PSS/GOPS and the pristine P(PyV)-H declined sharply (fig. S30, A to D). We also constructed inverters based on MNH-2 (8.6 wt %). The devices showed amplification characteristics similar

to those of inverters based on the pure semiconducting hydrogel. The maximum gain was 279 (Fig. 3I), and the power consumption was less than 3 μW (fig. S30E). The signal amplification function was good at low frequency but gradually decreased at high frequency (fig. S30F). Additionally, the device showed good operational stability, and its amplification properties remained basically unchanged during long time operation (Fig. 3J).

Semiconducting hydrogel for biosignal amplification

The outstanding semiconducting performance of these semiconducting hydrogels motivated our pursuit of their bioelectronic applications. The biocompatibility of the hydrogels was evaluated with cell viability tests by use of human keratinocyte cells (HaCaTs). Compared with conventional conjugated polymers with either hydrophilic or hydrophobic side chains, our semiconducting hydrogels showed low cytotoxicity and outstanding biocompatibility (Fig. 4A and figs. S31 and S32), probably because of their water processability and high water content nature. Thus, our semiconducting hydrogels might be suitable for in vivo applications. Traditional metal electrodes, such as gold (Au), often exhibit notably large interfacial impedance in aqueous solutions because of their limited ion conductance (*46*). By leveraging the high volumetric capacity of P(PyV)-H (485 F cm^{-3}), we were able to effectively reduce the impedance of the Au electrodes (fig. S33, A and B). Besides, conductive electrodes or those coated with conducting polymers are often used to record electrophysiological signals, but their signal-to-noise ratios (SNRs) are limited owing to the lack of on-site signal amplification. A single transistor has been used for amplifying biosignals (*47*). However, its current output characteristic is not compatible with existing voltage recording equipment for electrophysiological measurements, which impedes their applications (*48*).

We used both P(PyV)-H– and MNH-2–based inverter amplifiers for the amplification of electrooculography (EOG) and electrocardiograph (ECG) signals. The amplitude of EOG signals measured with commercial gel electrodes was below 1 mV. By contrast, the P(PyV)-H–based amplifier records voltages exceeding 200 mV (Fig. 4B and fig. S33C). When capturing ECG signals, both the MNH-2– and P(PyV)-H–based amplifiers display the typical P-QRS-T wave pattern of precordial leads V2 ECG signals (Fig. 4B and fig. S33D) (*49*). Compared with commercial gel electrodes, the hydrogel amplifiers produced output signals 40 times greater. Thus, circuits built with semiconducting hydrogels can simultaneously capture and amplify the electrophysiological signals. To demonstrate the SNR superiority of the MNH-2–based amplifiers, we also fabricated a small-size amplifier [channel width/length (W/L) = 10/10 μm] and a comparable-sized Au electrode (10 by 30 μm) (fig. S34, A and B). As shown in fig. S34C, the original data from the amplifier can depict the ECG signal with a clear PQR wave, despite the noise, and the SNR was 4.23 ± 0.37 dB, whereas the ECG signal acquired by the Au electrode was overwhelmed by noise, and the SNR was close to 0 dB. The distortion caused by different amplifications at different frequencies in the ECG signal can be rectified by applying compensation factors for different frequencies (fig. S34D).

Our hydrogel amplifiers can also be used for on-site recording of low-level biosignals, such as electroencephalogram (EEG), with minimal noise interference from cables and connections, providing high SNR. We fabricated flexible amplifiers for EEG recording (figs. S35 and S36). Before in vivo tests, we verified the amplification capability for the simulated EEG signals (Fig. 4C). Because of the interference of 50-Hz noise, the signal measured with the Au electrode has a low SNR, whereas our amplifier with the same effective area (0.012 mm^2) was less affected (Fig. 4D). After the signals were filtered with a 50-Hz notch filter, the signal obtained by our amplifier showed an amplification of more than 50 times and a high SNR of 15.8 dB, which is greater than the signals obtained with a conventional Au electrode (Fig. 4E and fig. S37).

On the basis of these results, both P(PyV)-H– and MNH-2–based amplifiers were used for recording the electrocorticogram (ECoG) signal of the cortex in vivo. The flexible hydrogel amplifier was placed on the dura mater of a mouse after craniectomy (Fig. 4F). With a silver/silver chloride (Ag/AgCl) electrode as the ground electrode and brain tissue as the electrolyte, the output of the amplifier can maintain a high gain under zero bias by adjusting the V_{DD} and source voltage (V_{SS}). The ECoG signals were recorded under both awake and anesthetized states of the mouse (fig. S38). The signal of the awake state was stronger than that under anesthesia. The same test was completed by using the Ag/AgCl electrode simultaneously, and the output of P(PyV)-H–based amplifier was more than 25 times stronger than that of the Ag/AgCl electrode with an area of 0.79 mm^2 (fig. S39). The awake ECoG signals obtained with the hydrogel amplifier and its time-frequency analysis diagram are shown in Fig. 4G. The ECoG signal amplitude increased after multiple sound stimuli, especially at high-frequency range, which is consistent with the previous studies based on an electrode array (*50*). For the MNH-2 amplifier, ECoG signals can be amplified but lost some high-frequency signals because of its lower cut-off frequency (fig. S40). Thus, MNHs have great potential in measuring low-frequency biological signals—such as EOG, ECG, and metabolite sensing—whereas P(PyV)-H is superior on relatively high-frequency signals such as EEG and ECoG.

We believe that there are three primary factors contributing to the varying amplifications observed in different types of electrical signal measurements. First, the slow ion migration rate makes the signal amplitude highly dependent on the signal frequency. The frequency difference of different electrophysiological signals affects the magnification of the device. Second, the interface impedance of different organisms is different, affecting the voltage drop on the device and thus the amplification of the device. Last, the ion concentration of the different biological tissues such as cerebrospinal fluid and body sweat is different, which affects the device's performance.

We have developed single- and multiple-network hydrogels that are based on a water-soluble n-type cationic semiconducting polymer. The hydrogels exhibit exceptional n-type semiconducting characteristics that can be used for constructing logic circuits and amplifiers. The semiconducting hydrogels exhibit good biocompatibility, mechanical properties, bioadhesion, and semiconducting properties. The semiconducting hydrogels are effective in amplifying various electrophysiological signals for bioelectronics.

REFERENCES AND NOTES

1. H. Yuk, J. J. Wu, X. H. Zhao, *Nat. Rev. Mater.* **7**, 935–952 (2022).
2. D.-A. Wang *et al.*, *Nat. Mater.* **6**, 385–392 (2007).
3. J. Li *et al.*, *Science* **357**, 378–381 (2017).
4. X. Zhao *et al.*, *Chem. Rev.* **121**, 4309–4372 (2021).
5. L. Su *et al.*, *Science* **377**, 213–218 (2022).
6. G. M. Taboada *et al.*, *Nat. Rev. Mater.* **5**, 310–329 (2020).
7. G. Tian *et al.*, *Adv. Mater.* **35**, e2212302 (2023).
8. D. J. Beebe *et al.*, *Nature* **404**, 588–590 (2000).
9. S. Nam, D. Mooney, *Chem. Rev.* **121**, 11336–11384 (2021).
10. Y. Gao *et al.*, *Nat. Commun.* **7**, 12316 (2016).
11. T. Ku *et al.*, *Nat. Biotechnol.* **34**, 973–981 (2016).
12. H. Yuk, B. Lu, X. Zhao, *Chem. Soc. Rev.* **48**, 1642–1667 (2019).
13. Q. Yang, Z. Hu, J. A. Rogers, *Acc. Mater. Res.* **2**, 1010–1023 (2021).
14. C. Yang, Z. Suo, *Nat. Rev. Mater.* **3**, 125–142 (2018).
15. S. J. K. O'Neill *et al.*, *Adv. Mater.* **35**, e2207634 (2023).
16. X. Liu, J. Liu, S. Lin, X. Zhao, *Mater. Today* **36**, 102–124 (2020).
17. S. R. Shin *et al.*, *ACS Nano* **7**, 2369–2380 (2013).
18. Y. Xu, K. Sheng, C. Li, G. Shi, *ACS Nano* **4**, 4324–4330 (2010).
19. Y. Hui *et al.*, *Nat. Electron.* **5**, 893–903 (2022).
20. Y. Wang *et al.*, *Nat. Synth.* **1**, 975–986 (2022).
21. G. J. Kim, K. O. Kim, *Sci. Rep.* **10**, 18858 (2020).
22. Y. Jiang *et al.*, *Nat. Biotechnol.* **41**, 652–662 (2023).
23. Y. Liu *et al.*, *Nat. Biotechnol.* **38**, 1031–1036 (2020).
24. P. Tan *et al.*, *Nat. Commun.* **13**, 358 (2022).
25. T. Zhu *et al.*, *Chem. Soc. Rev.* **52**, 473–509 (2023).
26. Y. Jiang, B. Tian, *Nat. Rev. Mater.* **3**, 473–490 (2018).
27. M. Fahlman *et al.*, *Nat. Rev. Mater.* **4**, 627–650 (2019).
28. H. J. Kim, B. Chen, Z. Suo, R. C. Hayward, *Science* **367**, 773–776 (2020).
29. R. C. Huber *et al.*, *J. Phys. Chem. B* **120**, 6215–6224 (2016).
30. D. Izuhara, T. M. Swager, *J. Am. Chem. Soc.* **131**, 17724–17725 (2009).
31. H. Tang *et al.*, *Nature* **611**, 271–277 (2022).
32. Z. Ke *et al.*, *J. Am. Chem. Soc.* **145**, 3706–3715 (2023).
33. S. Hwang *et al.*, *Phys. Chem. Chem. Phys.* **18**, 29199–29207 (2016).
34. J. Rivnay *et al.*, *Nat. Rev. Mater.* **3**, 17086 (2018).

35. S. Inal, G. G. Malliaras, J. Rivnay, *Nat. Commun.* **8**, 1767 (2017).
36. P. Li, J. Shi, Y. Lei, Z. Huang, T. Lei, *Nat. Commun.* **13**, 5970 (2022).
37. J. Yang *et al*., *Adv. Mater.* **29**, 1702115 (2017).
38. D. Wang, H. Yu, W. Shi, C. Xu, *Acc. Chem. Res.* **56**, 2127–2138 (2023).
39. H. Jia *et al*., *J. Mater. Chem. C Mater. Opt. Electron. Devices* **9**, 4927–4934 (2021).
40. H. Y. Wu *et al*., *Adv. Mater.* **34**, e2106235 (2022).
41. W. Huang *et al*., *Nature* **613**, 496–502 (2023).
42. T. Leydecker, Z. M. Wang, F. Torricelli, E. Orgiu, *Chem. Soc. Rev.* **49**, 7627–7670 (2020).
43. M. Zabihipour *et al*., *Adv. Mater. Technol.* **7**, 2101642 (2022).
44. S. M. Yu, C. J. Kousseff, C. B. Nielsen, *Synth. Met.* **293**, 117295 (2023).
45. H. Yuk *et al*., *Nature* **575**, 169–174 (2019).
46. Y. Liu *et al*., *Proc. Natl. Acad. Sci. U.S.A.* **115**, 11718–11723 (2018).
47. M. Wu *et al*., *Adv. Sci.* **10**, e2300504 (2023).
48. M. Braendlein, T. Lonjaret, P. Leleux, J. M. Badier, G. G. Malliaras, *Adv. Sci.* **4**, 1600247 (2016).
49. J. L. Garvey, *Emerg. Med. Clin. North Am.* **24**, 209–225, viii (2006).
50. M. Insanally *et al*., *J. Neural Eng.* **13**, 026030–26030 (2016).

ACKNOWLEDGMENTS

We acknowledge Molecular Materials and Nanofabrication Laboratory (MMNL) of Peking University for the use of instruments. We acknowledge Materials Processing and Analysis Center, Peking University, for the x-ray photoelectron spectroscopy measurement. We thank beamline BL14B1 (Shanghai Synchrotron Radiation Facility) for providing beamtime used for part of the x-ray scattering measurement. The computational part is supported by the High-Performance Computing Platform of Peking University. **Funding:** This work was supported by the National Natural Science Foundation of China, 92156019 (T.L.); National Natural Science Foundation of China, 22075001 (T.L.); Beijing Natural Science Foundation, JQ22006 (T.L.); National Natural Science Foundation of China, 22172085 (X.D.); National Natural Science Foundation of China, 52273114 (S.L.); National Natural Science Foundation of China, 52273170 (J.Z.); and the National Key R&D Program of China, 2022YFA1203200 (J.Z.). **Author contributions:** P.L. and W.S. contributed equally to this work. P.L., W.S., and T.L. conceived the idea and designed the experiments. J.L. and J.-P.C. synthesized the n-type polymer. P.L. performed the preparation of the hydrogels and the electronic device fabrication. W.S. performed flexible device fabrication. P.L. and W.S. performed logic device measurements. Y.L. and X.-Y.D. performed the DFT calculation. R.X. and J.Z. performed the band structure calculations. P.L. and K.L. performed AFM measurement. P.L. and Z.Z. performed the mechanical tests. X.L. supplied the p-type polymer. P.L. and X.W. performed SEM measurement. P.L., C.S., and Y.Z. performed EOG measurement. W.S., X.P., and J.X. performed ECG and EEG measurements. W.S., X.W., M.Y., and X.D. performed the in vivo ECoG measurement. Z.M., G.J., and S.L. performed the cell experiment. P.L., W.S. and T.L. wrote the manuscript. All the authors reviewed and approved the manuscript. **Competing interests:** P.L., W.S., J.L., J.-P.C., X.-Y.D., and T.L. filed China National Intellectual Property Administration provisional patent applications related to this work (applications nos. 202311326854.4, filed 13 October 2023, nos. 202311333469.2, filed 16 October 2023). The other authors declare that they have no competing interests. **Data and materials availability:** All data are available in the main text or the supplementary materials.

SUPPLEMENTARY MATERIALS

science.org/doi/10.1126/science.adj4397
Materials and Methods
Supplementary Text
Figs. S1 to S45
Tables S1 to S3
MDAR Reproducibility Checklist

Submitted 27 June 2023; resubmitted 17 January 2024
Accepted 13 March 2024
10.1126/science.adj4397